

# Energy & Environmental Science

Accepted Manuscript



This is an *Accepted Manuscript*, which has been through the Royal Society of Chemistry peer review process and has been accepted for publication.

*Accepted Manuscripts* are published online shortly after acceptance, before technical editing, formatting and proof reading. Using this free service, authors can make their results available to the community, in citable form, before we publish the edited article. We will replace this *Accepted Manuscript* with the edited and formatted *Advance Article* as soon as it is available.

You can find more information about *Accepted Manuscripts* in the [Information for Authors](#).

Please note that technical editing may introduce minor changes to the text and/or graphics, which may alter content. The journal's standard [Terms & Conditions](#) and the [Ethical guidelines](#) still apply. In no event shall the Royal Society of Chemistry be held responsible for any errors or omissions in this *Accepted Manuscript* or any consequences arising from the use of any information it contains.

# Mechanistic Insights into Solar Water Oxidation by Cobalt-Phosphate-Modified $\alpha$ -Fe<sub>2</sub>O<sub>3</sub> Photoanodes

Gerard M. Carroll, Diane K. Zhong, Daniel R. Gamelin\*

**Abstract:** Interfacing  $\alpha$ -Fe<sub>2</sub>O<sub>3</sub> photoanodes with the water-oxidation electrocatalyst Co-Pi is known to enhance their photon-to-current conversion efficiencies by reducing electron-hole recombination near their surfaces, particularly at more negative potentials, but the mechanism by which Co-Pi modification achieves this enhancement remains poorly understood. Conflicting experimental observations have been recorded with respect to the role of Co-Pi thickness and even the participation of Co-Pi in catalysis, raising important general questions concerning the fundamental properties of catalyst-modified PEC water-oxidation photoanodes for solar energy conversion. Here, we report results from electrochemical, spectroscopic, and microscopic measurements on mesostructured Co-Pi/ $\alpha$ -Fe<sub>2</sub>O<sub>3</sub> composite photoanodes that reveal evolving pathways of water oxidation with increasing Co-Pi thickness. These results highlight major fundamental differences between structured and planar Co-Pi/ $\alpha$ -Fe<sub>2</sub>O<sub>3</sub> composite photoanodes and help to reconcile previously conflicting mechanistic interpretations.

## Introduction

Photoelectrochemical (PEC) water splitting into hydrogen and oxygen is a promising strategy for capturing and storing the abundant solar energy incident upon the Earth's surface.<sup>1-6</sup> Photoelectrolysis of water poses significant technical challenges, however. The oxidation half reaction is a four-proton, four-electron process that typically requires a large overpotential.<sup>1-6</sup> Additionally, PEC photoelectrodes must be efficient, stable under operating conditions, able to absorb a large fraction of the visible spectrum, possess properly aligned band edges for thermodynamically favorable charge transfer, and be cost effective.<sup>4, 5, 7</sup> To date, no single material has demonstrated all of these characteristics.

With a band gap of 2.1 eV, stability under operating conditions, and a valence-band potential  $\sim$ 1.6 V more positive than the thermodynamic water-oxidation potential (+1.23 V vs RHE), hematite ( $\alpha$ -Fe<sub>2</sub>O<sub>3</sub>) continues to attract attention as a model photoanode for PEC water oxidation.<sup>7-11</sup> Owing to poor charge mobility ( $10^{-2}$  to  $10^{-1}$  cm<sup>2</sup>s<sup>-1</sup>V<sup>-1</sup>),<sup>12</sup> short hole-diffusion lengths (2-20 nm),<sup>13, 14</sup> and slow charge-transfer kinetics ( $10^{-3}$  sec to 1 sec),<sup>15-22</sup> however, the solar-to-hydrogen efficiencies achieved with  $\alpha$ -Fe<sub>2</sub>O<sub>3</sub> photoelectrodes suffer greatly from electron-hole recombination, both within the bulk and at the semiconductor liquid junction (SCLJ).

Several strategies have been explored to reduce bulk electron-hole recombination in  $\alpha$ -Fe<sub>2</sub>O<sub>3</sub>, including doping with Si, Ti, Al, Ge, Sn, and Nb<sup>23-28</sup> and nano-structuring.<sup>9, 23-26, 29-33</sup> Similarly, several groups have explored interfacing  $\alpha$ -Fe<sub>2</sub>O<sub>3</sub> with water-oxidation catalysts to reduce surface electron-hole recombination.<sup>8, 15, 34-36</sup> In particular, the earth-abundant, self-healing water-oxidation electrocatalyst known as cobalt phosphate (Co-Pi)<sup>37, 38</sup> has received enormous attention since initial observations of water-oxidation onsets shifted to more negative potentials in Co-Pi/ $\alpha$ -Fe<sub>2</sub>O<sub>3</sub> composite photoanodes.<sup>8, 34, 39</sup> As a "self-healing" catalyst,<sup>38</sup> Co-Pi has practical advantages over other molecular or nanocrystalline catalysts, which may degrade or dissociate from the photoanode surface over time.

Since first reported,<sup>34</sup> numerous studies have addressed optimization and mechanistic probing of the Co-Pi/ $\alpha$ -Fe<sub>2</sub>O<sub>3</sub> interface.<sup>8, 15, 39-42</sup> Interestingly, these studies have generated seemingly incompatible models to explain the nature of the Co-Pi photocurrent enhancement on  $\alpha$ -Fe<sub>2</sub>O<sub>3</sub> photoanodes. For example, some of the most detailed insights into this interface have come from studies of planar Co-Pi/ $\alpha$ -Fe<sub>2</sub>O<sub>3</sub> "model" systems<sup>41</sup> but the experimental results from these model systems haven't been in full agreement with those from PEC studies of high-surface-area Co-Pi/ $\alpha$ -Fe<sub>2</sub>O<sub>3</sub> composite photoanodes.<sup>8, 39</sup> Specifically, photoelectrochemical measurements on mesostructured  $\alpha$ -Fe<sub>2</sub>O<sub>3</sub> photoanodes have

indicated an optimal Co-Pi thickness of only  $<10$  nm, beyond which the PEC performance actually diminished because of a "kinetic bottleneck".<sup>8, 39</sup> In contrast, analogous PEC measurements on planar  $\alpha$ -Fe<sub>2</sub>O<sub>3</sub> photoanodes have showed continued PEC improvement with increasing Co-Pi thickness up to as thick as 425 nm.<sup>41</sup> One hypothesis<sup>41</sup> to explain these contradictory observations is that the latter measurements involved backside illumination (*i.e.*, through the substrate and  $\alpha$ -Fe<sub>2</sub>O<sub>3</sub>, Figure 2a), whereas the former involved frontside illumination (*i.e.*, through the Co-Pi); Frontside illumination is potentially subject to parasitic photon absorption by the Co-Pi itself,<sup>43</sup> introducing new absorption losses with increasing Co-Pi thickness. This hypothesis has never been tested, and the stark contrast between mesostructured and planar Co-Pi/ $\alpha$ -Fe<sub>2</sub>O<sub>3</sub> composite photoanodes thus remains unexplained. Additionally, transient absorption measurements on mesostructured Co-Pi/ $\alpha$ -Fe<sub>2</sub>O<sub>3</sub> composite photoanodes have revealed photogenerated holes with extended lifetimes apparently within the  $\alpha$ -Fe<sub>2</sub>O<sub>3</sub> itself, leading to the suggestion that Co-Pi does not directly participate in water-oxidation catalysis but instead plays an indirect role by inducing additional  $\alpha$ -Fe<sub>2</sub>O<sub>3</sub> band bending that reduces electron-hole recombination.<sup>40, 44</sup> This suggestion appears incompatible with observations of an "adaptive junction" formed between  $\alpha$ -Fe<sub>2</sub>O<sub>3</sub> and Co-Pi or related catalysts,<sup>42, 45</sup> and of capacitive hole storage within the Co-Pi layer.<sup>41</sup> These mechanistic contrasts also remain unresolved. Further mechanistic studies of PEC water oxidation by Co-Pi/ $\alpha$ -Fe<sub>2</sub>O<sub>3</sub> composite photoanodes are required to reconcile these divergent understandings of this important interface.

Here, we assess the influence of Co-Pi layer thickness on the PEC performance of mesostructured  $\alpha$ -Fe<sub>2</sub>O<sub>3</sub> photoanodes with the aim of consolidating the understanding of the role of Co-Pi in enhancing PEC water oxidation by  $\alpha$ -Fe<sub>2</sub>O<sub>3</sub> photoanodes. The results demonstrate the existence of an optimal Co-Pi thickness that is rather small ( $\sim 2.5$  nm, estimated from Coulometry) and independent of the illumination direction, confirming a non-trivial origin of the diminished PEC performance with thicker Co-Pi catalyst layers. This bottleneck with thick Co-Pi layers is proposed to stem from the texturing of these mesostructured  $\alpha$ -Fe<sub>2</sub>O<sub>3</sub> photoanodes, which enhances surface electron-hole recombination relative to planar  $\alpha$ -Fe<sub>2</sub>O<sub>3</sub> photoanodes. Furthermore, mechanistic insights gained from measuring the pH dependence of this PEC activity as a function of Co-Pi thickness reveal that at large Co-Pi thicknesses, all water oxidation proceeds via Co-Pi, whereas at the optimal Co-Pi thickness, charge transfer to water occurs through Co-Pi-catalyzed water oxidation *and* by direct  $\alpha$ -Fe<sub>2</sub>O<sub>3</sub> water oxidation, the relative importance of each pathway changing with applied potential. These findings shed new light on the role Co-Pi plays in improving the performance of these and related solar water-splitting photoanodes, and highlight fundamentally important contrasts between planar and structured composite photoanodes.

## Experimental

Mesostructured  $\alpha$ -Fe<sub>2</sub>O<sub>3</sub> photoanodes were fabricated on fluorine doped tin oxide (FTO) coated glass (TEC 15, Hartford Glass Co.) by an atmospheric pressure chemical vapor deposition (APCVD) method described previously.<sup>8, 33, 39</sup> The APCVD synthesis was modified to optimize  $\alpha$ -Fe<sub>2</sub>O<sub>3</sub> for backside illumination photocurrent densities by decreasing the deposition period to  $\sim 70\%$  of the typical deposition time, and thus producing thinner  $\alpha$ -Fe<sub>2</sub>O<sub>3</sub> films. To fabricate the Co-Pi/ $\alpha$ -Fe<sub>2</sub>O<sub>3</sub> composite photoanodes, Co-Pi was deposited onto  $\alpha$ -Fe<sub>2</sub>O<sub>3</sub> photoanodes by photo-assisted electrodeposition under AM1.5 simulated solar irradiation from the back of the sample (through the FTO). All Co-Pi depositions were carried out at a constant current of  $6 \mu\text{A}/\text{cm}^2$  from a solution of 0.5 mM cobalt nitrate in 0.1 M potassium phosphate buffer at pH 8. The Co-Pi thickness was controlled by varying the amount charge passed, *i.e.*, the duration of deposition. Co-Pi thicknesses are reported as the average values estimated from the charges passed during deposition. Co-Pi dissolution was achieved by submerging Co-Pi/ $\alpha$ -Fe<sub>2</sub>O<sub>3</sub> composite photoanodes in fresh aqueous 0.1M KPi (pH 8) solutions for fixed times.

Photoelectrochemical (PEC) and electrochemical (EC) measurements were conducted in a three-electrode configuration, with the photoanode as the working electrode, Ag/AgCl as the reference electrode, and Pt as the counter electrode. A Gamry Series G 300 potentiostat with a frequency response analyzer was used for all measurements. Unless otherwise stated, all PEC measurements were performed in 0.1M KPi (pH8) using backside illumination (through the FTO, Figure 2a) with calibrated 1 sun AM 1.5 simulated sunlight irradiation using an Oriel 96000 solar simulator equipped with a 150 W Xenon arc lamp and an Oriel AM 1.5 filter. Potentials vs the reversible hydrogen electrode (RHE) were calculated using the Nernst equation as  $E_{\text{RHE}} = E_{\text{Ag/AgCl}} + 0.0591(\text{pH}) + 0.1976 \text{ V}$ . All photocurrent-voltage and current-voltage data were collected at a scan rate of 10 mV/s. Masks with 6 mm diameter apertures were applied onto all working electrodes for defined active surface areas.

Galvanostatic pH-dependent PEC measurements were performed by titrating aqueous 0.5M KPi (pH 5) with aqueous 0.1M KOH. Incident photon-to-current conversion efficiency (IPCE) data were collected using a 250 W tungsten light source directed through an Oriel Cornerstone 74000 monochromator blazed at 350 nm. Spectral efficiency was calculated using the equation:  $\text{IPCE}(\lambda) = 1240 \cdot \text{Current}(\text{A}) / \text{Power}(\text{W}) \cdot \lambda(\text{nm})$ . Light intensity was measured with a calibrated silicon detector with a maximum light output of  $\sim 6 \text{ mW}/\text{cm}^2$  at 540 nm. The steady-state dark current was collected prior to each IPCE measurement and was subtracted from the resulting spectrum. Scanning electron microscopy (SEM) images were collected using an FEI Sirion SEM at an accelerating voltage of 15 keV.

## Results and Analysis

Figure 1 compares scanning electron microscopy (SEM) images of an  $\alpha$ -Fe<sub>2</sub>O<sub>3</sub> photoanode collected before and after photo-assisted electrochemical deposition of Co-Pi with backside illumination. Whereas photo-assisted electrochemical deposition of Co-Pi onto  $\alpha$ -Fe<sub>2</sub>O<sub>3</sub> mesostructures using frontside illumination has previously been shown to yield uniform catalyst coverage across the entire  $\alpha$ -Fe<sub>2</sub>O<sub>3</sub> surface,<sup>8</sup> Co-Pi deposition via backside illumination has not been explored. The bare  $\alpha$ -Fe<sub>2</sub>O<sub>3</sub> photoanode displays a highly structured surface with resolvable features on the order of ~10 nm in diameter, typical for mesostructured  $\alpha$ -Fe<sub>2</sub>O<sub>3</sub> photoanodes prepared by APCVD.<sup>33</sup> Following Co-Pi deposition, the smallest resolvable features grow to ~30 nm. Assuming an average volume of ~125 Å<sup>3</sup> per CoO<sub>6</sub> subunit,<sup>46</sup> and an  $\alpha$ -Fe<sub>2</sub>O<sub>3</sub> surface roughness factor of 20,<sup>33</sup> an average Co-Pi thickness of ~25 nm can be estimated from the charge passed during deposition to make the composite photoanode in Figure 1b. Although it is difficult to extract the exact Co-Pi thickness from SEM, the loss of resolvable microstructure in Figure 1b is consistent with this estimated thickness.

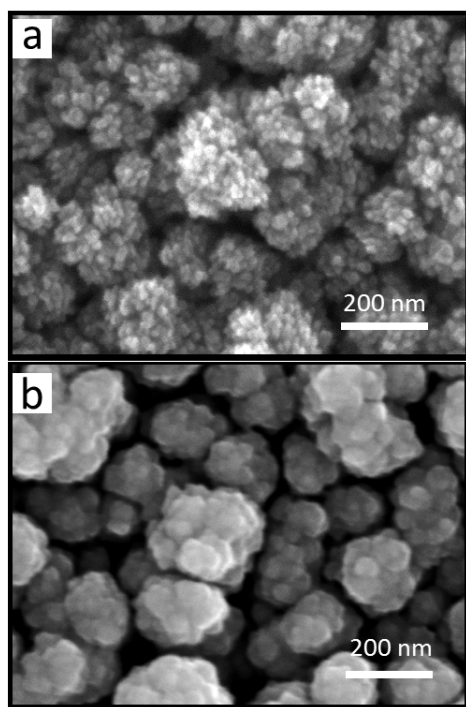


**Figure 1.** Scanning electron microscope images of (a) a bare mesostructured  $\alpha$ -Fe<sub>2</sub>O<sub>3</sub> photoanode, and (b) the same photoanode following deposition of a ~25 nm thick layer of Co-Pi via photo-assisted electrochemical deposition using backside illumination. The viewing angle is normal to the sample surface.

Figure 2b describes the photocurrent density–voltage ( $J$ - $V$ ) characteristics of an  $\alpha$ -Fe<sub>2</sub>O<sub>3</sub> photoanode whose surface has been modified by deposition of a thick (~25 nm) layer of Co-Pi,

illuminated with 1 sun, AM1.5 simulated sunlight from the back side. Remarkably, the onset potential for PEC water oxidation is approximately the same with and without the thick Co-Pi layer. The photocurrent density measured at +1.8 V is greater for the Co-Pi/ $\alpha$ -Fe<sub>2</sub>O<sub>3</sub> photoanode than for the parent  $\alpha$ -Fe<sub>2</sub>O<sub>3</sub> photoanode, but close inspection reveals that this enhancement arises from direct electrocatalysis by Co-Pi (Fig. 2b, inset), instead of from enhanced photoelectrocatalysis as desired. Subtracting the steady state dark current yields a photocurrent density of only 1.2 mA/cm<sup>2</sup> at +1.8 V for the composite photoanode, well below that of the parent  $\alpha$ -Fe<sub>2</sub>O<sub>3</sub> photoanode (1.5 mA/cm<sup>2</sup> at +1.8 V). Interfacing with a ~25 nm Co-Pi layer thus actually diminishes the PEC performance of mesostructured  $\alpha$ -Fe<sub>2</sub>O<sub>3</sub> photoanodes under backside illumination, confirming previous observations of a kinetic bottleneck in this regime.

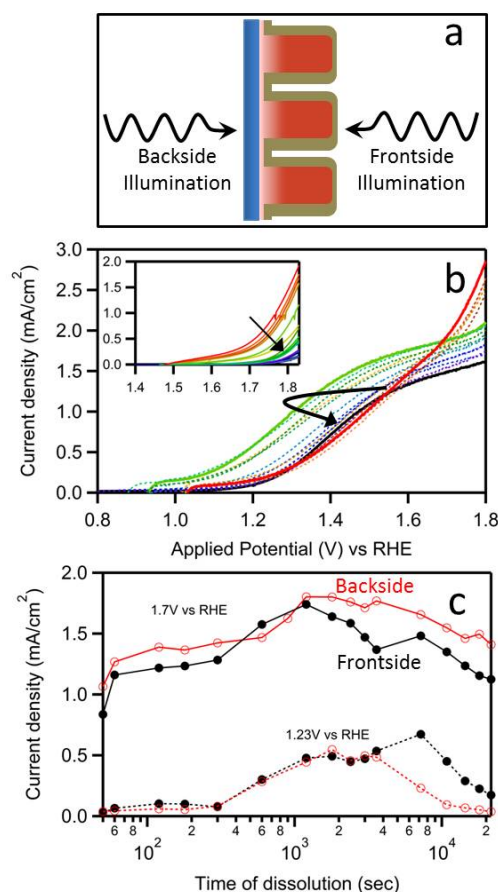


**Figure 2.** (a) Schematic illustration of front- and backside illumination. (b)  $J$ - $V$  scans under simulated 1 sun AM 1.5 backside illumination of a bare  $\alpha$ -Fe<sub>2</sub>O<sub>3</sub> electrode (black) and following Co-Pi deposition (red, ~25 nm thick). Intermediate colors from orange to blue show the  $J$ - $V$  scans of the same electrode after 1|3|5|10|15|20|30|40|50|60|120|240|360|480|600 minutes of Co-Pi dissolution in fresh 0.1M KPi (pH 8) electrolyte solution. The solid lines correspond to minima (bare  $\alpha$ -Fe<sub>2</sub>O<sub>3</sub>, and with ~25 nm-thick Co-Pi) and the maximum (after 30 min dissolution). Inset: Dark current response of the same anode at each of the same stages of Co-Pi dissolution. (c) Steady-state photocurrent densities (steady-state dark current subtracted) for front (black, closed circles) and backside (red, open circles) illumination measured at +1.7 V (solid) and +1.23 V (dashed) vs RHE. All data were collected using 0.1M KPi (pH 8) buffer.

Co-Pi slowly disproportionates and dissolves in cobalt-free electrolyte under open-circuit conditions.<sup>38</sup> Here, we show that this dissolution can be used to optimize the Co-Pi thickness in Co-Pi/ $\alpha$ -Fe<sub>2</sub>O<sub>3</sub> composite photoanodes. To illustrate this optimization, a series of PEC measurements was performed on the same photoanode in cobalt-free electrolyte, with deliberate Co-Pi dissolution steps performed between each pair of  $J$ - $V$  measurements. Specifically, the composite photoelectrode was transferred to a cobalt-free aqueous solution following each PEC measurement, where dissolution was allowed to proceed for a fixed time, and the photoelectrode was then transferred back into the PEC cell and its  $J$ - $V$  response measured again. From the initial thickness of  $\sim$ 25 nm (red trace), Figure 2b shows that the onset potential shifts to more *negative* potentials with Co-Pi dissolution until a maximum shift is reached at  $\sim$ 30 min dissolution time (green trace). Further dissolution then shifts the onset potential to more positive potentials again, until eventually all of the Co-Pi has been removed and the  $J$ - $V$  curve converges on that of the parent  $\alpha$ -Fe<sub>2</sub>O<sub>3</sub> photoanode, measured prior to any Co-Pi deposition. From the inset in Figure 2b, the dark current density does not follow the same trend; its onset potential only increases with Co-Pi dissolution. Figure 2c summarizes steady-state photocurrent density data (see Supporting Information) measured with both front- and backside illumination at +1.7 V and +1.23 V as a function of Co-Pi dissolution time. Both the front- and backside PEC follow the same trend, proceeding through a maximum at  $\sim$ 30 min dissolution. This trend illustrates the "kinetic bottleneck" effect described previously,<sup>39</sup> but here is demonstrated with backside illumination. This result eliminates nonproductive photon absorption by Co-Pi as a viable hypothesis to explain the reduced PEC performance of composite Co-Pi/ $\alpha$ -Fe<sub>2</sub>O<sub>3</sub> photoanodes having thick Co-Pi layers.

Figure 3 shows incident-photon-to-current-conversion-efficiency (IPCE) curves measured for the same  $\alpha$ -Fe<sub>2</sub>O<sub>3</sub> photoanode with various Co-Pi thicknesses. The bare  $\alpha$ -Fe<sub>2</sub>O<sub>3</sub> photoanode shows a typical response, with its photocurrent onset at the  $\alpha$ -Fe<sub>2</sub>O<sub>3</sub> absorption edge ( $\lambda \approx$  600 nm) and a maximum of 14% at  $\lambda =$  450 nm. The decreasing IPCE at even shorter wavelengths is typical for backside illumination, and reflects bulk-recombination losses of photo-generated charge carriers created near the  $\alpha$ -Fe<sub>2</sub>O<sub>3</sub>/FTO interface. Deposition of a thin Co-Pi layer ( $\sim$ 2.3 nm) onto this photoanode's surface increases the IPCE values at all wavelengths, yielding a maximum of  $\sim$ 19% at 445 nm. Addition of more Co-Pi (to  $\sim$ 9.7 nm thick) causes a decrease in IPCE throughout the entire spectral window, however, and the IPCE curve is almost indistinguishable from that of the bare photoanode. Even further Co-Pi addition (to  $\sim$ 25 nm) decreases the IPCE values yet further, yielding an IPCE maximum of only 7% at  $\lambda =$  445 nm. The uniform decrease in IPCE with thick Co-Pi deposition differs from what would be expected if this large reduction in PEC performance came from photon absorption by Co-Pi (dotted curve, transmittance), further arguing against the hypothesis of substantial non-productive light absorption by the catalyst. Instead, the results presented here indicate that a more

complex and fundamentally important limitation is encountered with thick Co-Pi layers.

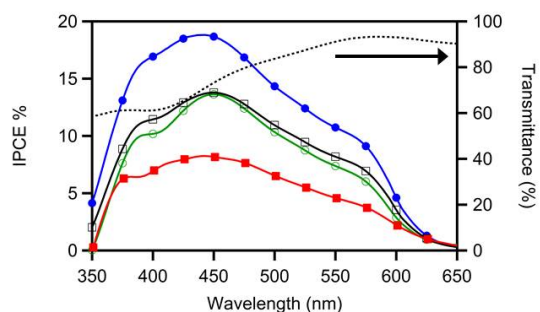


**Figure 3.** Incident photon to current conversion efficiency (IPCE) spectra for bare (black, open square), 2.3 nm (blue, closed circle), 9.7 nm (green, open circle) and 25 nm (red, closed square) thick Co-Pi on  $\alpha$ -Fe<sub>2</sub>O<sub>3</sub> in 0.1 M KPi at 1.7 V vs. RHE from backside illumination. For reference, the dashed line shows the transmittance spectrum of a  $\sim$ 25 nm thick Co-Pi layer deposited on FTO.

In our experiments, the optimized thicknesses of the APCVD  $\alpha$ -Fe<sub>2</sub>O<sub>3</sub> photoanodes themselves for front- and backside illumination are  $\sim$ 600 and  $\sim$ 450 nm, respectively. Figure 4 shows  $J$ - $V$  curves measured for two Co-Pi/ $\alpha$ -Fe<sub>2</sub>O<sub>3</sub> composite photoelectrodes, with  $\alpha$ -Fe<sub>2</sub>O<sub>3</sub> growth optimized for either front ( $\sim$ 600 nm thick) or backside ( $\sim$ 450 nm thick) illumination. Figure 4a shows that the thicker  $\alpha$ -Fe<sub>2</sub>O<sub>3</sub> photoanode achieves a lower plateau current density ( $\sim$ 1 mA/cm<sup>2</sup>) than the thinner one ( $\sim$ 2 mA/cm<sup>2</sup>) under backside illumination. Upon deposition of  $\sim$ 25 nm (average) Co-Pi onto these two photoanodes, the photocurrent onset potential of the thicker photoanode shifts to more *negative* potentials by  $\sim$ 200 mV, whereas that of the thinner photoanode actually shifts to more *positive* potentials. A close inspection of the SEM image of this Co-Pi/ $\alpha$ -Fe<sub>2</sub>O<sub>3</sub> photoelectrode (Figure 4a, inset) reveals that backside photo-assisted electrodeposition does not uniformly deposit Co-Pi onto the surface of the thicker  $\alpha$ -Fe<sub>2</sub>O<sub>3</sub> photoanode. The nodules still show their fine microstructure whereas the dark regions in the valleys now appear flat, suggesting that Co-Pi deposits preferentially in the valleys. This result implies that the PEC activity of the thicker  $\alpha$ -Fe<sub>2</sub>O<sub>3</sub> photoanode is restricted to these valleys when using backside illumination, and the high-surface-area nodules do not participate equally. This loss of active surface area causes the thicker  $\alpha$ -Fe<sub>2</sub>O<sub>3</sub> photoelectrodes to behave like planar  $\alpha$ -Fe<sub>2</sub>O<sub>3</sub> photoanodes when interfaced with Co-Pi, showing continued shifting to more negative potentials of the onset potential even with application of thick Co-Pi layers (Figure 4a).<sup>41</sup> In contrast, the thinner  $\alpha$ -Fe<sub>2</sub>O<sub>3</sub> photoanode shows evidence of substantial Co-Pi deposition onto the high-surface-area nodules (Figure 4b, inset) even with backside illumination, showing that the full surface area participates in water oxidation, as desired. In this limit, thick Co-Pi layers impair PEC performance (Figure 4b).

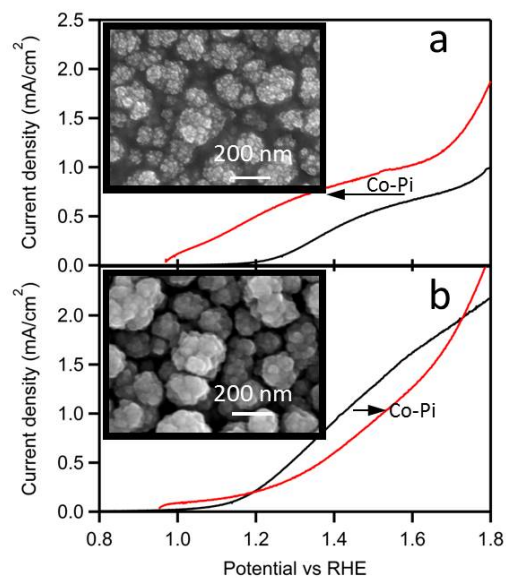


**Figure 4.** *J-V* scans for bare (black) and  $\sim 25$  nm Co-Pi-coated (red)  $\alpha$ -Fe<sub>2</sub>O<sub>3</sub> photoanodes measured in 0.1 M KPi (pH 8) with backside illumination. **(a)** Co-Pi/ $\alpha$ -Fe<sub>2</sub>O<sub>3</sub> optimized for frontside illumination ( $\sim 600$  nm thick  $\alpha$ -Fe<sub>2</sub>O<sub>3</sub>). **(b)** Co-Pi/ $\alpha$ -Fe<sub>2</sub>O<sub>3</sub> optimized for backside illumination ( $\sim 450$  nm thick  $\alpha$ -Fe<sub>2</sub>O<sub>3</sub>). The insets show SEM images of the two Co-Pi/ $\alpha$ -Fe<sub>2</sub>O<sub>3</sub> photoelectrodes.

We now turn to the water oxidation catalysis itself. To probe this chemistry, galvanostatic pH titrations were conducted under illumination for four different Co-Pi thicknesses at two different current densities on the same 450 nm thick  $\alpha$ -Fe<sub>2</sub>O<sub>3</sub> photoanode (Fig. 5). As an electrocatalyst, Co-Pi is known to proceed through a proton-coupled electron-transfer step that precedes the rate-limiting O-O bond formation step.<sup>46</sup> This mechanism yields a Nernstian pH dependence of  $-59$  mV/pH. A pH dependence of  $\sim -59$  mV/pH would therefore be expected for a Co-Pi/ $\alpha$ -Fe<sub>2</sub>O<sub>3</sub> composite photoanode if PEC water oxidation proceeds exclusively via the Co-Pi electrocatalyst. For reference, the bare  $\alpha$ -Fe<sub>2</sub>O<sub>3</sub> photoanode was measured and shows a pH dependence of  $-97$  mV/pH under AM 1.5 illumination from the backside (at both  $35$  and  $700$   $\mu$ A/cm<sup>2</sup>, Figure 5). Addition of  $0.6$  nm Co-Pi onto the bare  $\alpha$ -Fe<sub>2</sub>O<sub>3</sub> photoanode changes the pH dependence from  $-97$  to  $-82$  mV/pH at  $35$   $\mu$ A/cm<sup>2</sup>, and  $-95$  mV/pH at  $700$   $\mu$ A/cm<sup>2</sup>. These changes indicate that Co-Pi is modifying the mechanism of water oxidation in these composite photoanodes, but does so more at low potentials (low currents) than at high potentials (higher currents). Further addition of Co-Pi continues to decrease the pH dependence until, at a Co-Pi thickness of  $\sim 25$  nm, the slopes of both the  $35$  and  $700$   $\mu$ A/cm<sup>2</sup> data sets are both close to  $-59$  mV/pH, *i.e.*, both resemble the inverse first order dependence on proton activity anticipated from water-oxidation catalysis by Co-Pi. Co-Pi/ $\alpha$ -Fe<sub>2</sub>O<sub>3</sub> composite photoanodes with thick Co-Pi catalyst layers thus appear to oxidize water solely via the Co-Pi electrocatalyst.

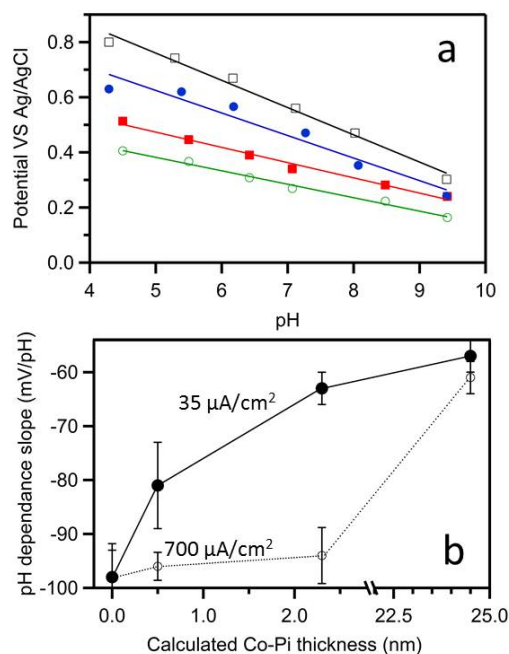


**Figure 5.** **(a)** Galvanostatic pH titration taken at  $35$   $\mu$ A/cm<sup>2</sup> of bare  $\alpha$ -Fe<sub>2</sub>O<sub>3</sub> (black, open square),  $0.62$  nm Co-Pi/ $\alpha$ -Fe<sub>2</sub>O<sub>3</sub> (blue, closed circle),  $2.3$  nm Co-Pi/ $\alpha$ -Fe<sub>2</sub>O<sub>3</sub> (green, open circle) and  $\sim 25$  nm Co-Pi/ $\alpha$ -Fe<sub>2</sub>O<sub>3</sub> (red, closed square) in  $0.5$  M KPi under AM1.5 illumination from the backside. All pH data were collected on the same  $450$  nm thick  $\alpha$ -Fe<sub>2</sub>O<sub>3</sub> sample. **(b)** The fitted slopes from the galvanostatic pH titrations at  $35$   $\mu$ A/cm<sup>2</sup> (closed circles, solid line) and  $700$   $\mu$ A/cm<sup>2</sup> (open circles, dotted line) plotted vs Co-Pi thickness. Error bars indicate the uncertainty associated with the linear fit to the pH data.

The above data show that Co-Pi/ $\alpha$ -Fe<sub>2</sub>O<sub>3</sub> composite photoanodes prepared with the optimized Co-Pi thickness ( $\sim 2.3$  nm) exhibit a pH dependence that is intermediate between those of the bare  $\alpha$ -Fe<sub>2</sub>O<sub>3</sub> and thick-composite photoelectrodes. This intermediate regime is interpreted as reflecting a superposition of two mechanisms (see Supporting Information), one involving water oxidation directly at the  $\alpha$ -Fe<sub>2</sub>O<sub>3</sub> surface ( $-97$  mV/pH) and the other water oxidation by Co-Pi ( $-59$  mV/pH). The degree to which each mechanism participates varies with current density and hence with applied potential. At low potential (current), the majority of oxygen evolution occurs via Co-Pi, but at higher potentials (currents) the  $\alpha$ -Fe<sub>2</sub>O<sub>3</sub> surface mechanism dominates. The optimized Co-Pi/ $\alpha$ -Fe<sub>2</sub>O<sub>3</sub> composite photoanodes thus rely on Co-Pi catalysis for activity at low potentials and on direct  $\alpha$ -Fe<sub>2</sub>O<sub>3</sub> water oxidation for activity at high potentials. To our knowledge, this result constitutes the first mechanistic evidence of water oxidation by Co-Pi in such composite photoanodes.

## Discussion

Co-Pi can be described as forming an "adaptive Schottky junction"<sup>42, 45</sup> with the surface of the underlying  $\alpha$ -Fe<sub>2</sub>O<sub>3</sub> photoelectrode, in which the open circuit voltage and quasi-Fermi level splitting increase upon oxidation of the ion permeable electrocatalyst, increasing the driving force for electron-hole separation and reducing surface recombination. From this description, it is expected that increasing the thickness of Co-Pi should only improve the  $J$ - $V$  characteristics of the composite photoelectrode. Such behavior is indeed observed in planar Co-Pi/ $\alpha$ -Fe<sub>2</sub>O<sub>3</sub> photoanodes,<sup>41</sup> but it is not observed with mesostructured Co-Pi/ $\alpha$ -Fe<sub>2</sub>O<sub>3</sub> photoanodes.<sup>8, 39</sup> Although mesostructured  $\alpha$ -Fe<sub>2</sub>O<sub>3</sub> photoanodes yield substantially higher photocurrent densities than planar  $\alpha$ -Fe<sub>2</sub>O<sub>3</sub> photoanodes, the PEC performance of mesostructured Co-Pi/ $\alpha$ -Fe<sub>2</sub>O<sub>3</sub> composite photoanodes maximizes at an intermediate Co-Pi thickness, implicating the existence of a new process that limits the overall performance.

We attribute this new limiting process (the "kinetic bottleneck"<sup>39</sup>) to increased interfacial recombination between conduction-band electrons and Co-Pi holes with increasing Co-Pi layer thickness in the mesostructures, ultimately arising from the inability to sweep electrons away from the SCLJ because of the  $\alpha$ -Fe<sub>2</sub>O<sub>3</sub> texturing. This interpretation is summarized in Figure 6a. Electron diffusion in a planar  $\alpha$ -Fe<sub>2</sub>O<sub>3</sub> photoanode is largely perpendicular to (away from) the SCLJ (Figure 6a, left). Increasing the surface area of an  $\alpha$ -Fe<sub>2</sub>O<sub>3</sub> photoanode increases the distance that photogenerated electrons must travel before they are no longer in proximity to this interface. Much of this added distance is actually parallel to the SCLJ (Figure 6a, right). The probability of electron recombination with holes stored within the Co-Pi layer increases in proportion to the time

the electrons must reside near the SCLJ. This contrast results in the existence of the kinetic bottleneck only in highly structured Co-Pi/ $\alpha$ -Fe<sub>2</sub>O<sub>3</sub> composite photoanodes, and only when the entire high surface area participates in the photoelectrocatalysis (Figure 4).

The pH data presented here (Figure 5) indicate that water-oxidation catalysis proceeds exclusively *via* Co-Pi when the Co-Pi layer is thick. Under these conditions, however, many oxidizing equivalents are stored in the Co-Pi layer at steady state, and surface electron-hole recombination in mesostructured photoanodes becomes overwhelmingly problematic. For mesostructured Co-Pi/ $\alpha$ -Fe<sub>2</sub>O<sub>3</sub> composite photoanodes, PEC performance is therefore optimized when the Co-Pi layer is thin. Interestingly, in these optimized mesostructured Co-Pi/ $\alpha$ -Fe<sub>2</sub>O<sub>3</sub> composite photoanodes, water-oxidation catalysis proceeds *via* Co-Pi at low potentials but directly *via* the  $\alpha$ -Fe<sub>2</sub>O<sub>3</sub> surface at high potentials. In this way, Co-Pi improves the performance of mesostructured  $\alpha$ -Fe<sub>2</sub>O<sub>3</sub> photoanodes by catalyzing water oxidation at the lowest potentials, shifting their onset potentials more negative as desired for practical applications. These conclusions are summarized graphically in Figure 6b and highlight the important fundamental differences between mesostructured and planar PEC photoanodes for solar water oxidation. Importantly, these results shed new light onto the longstanding uncertainty about whether Co-Pi is an active catalyst or merely a spectator in such photoelectrochemistry.<sup>47</sup> Because of the marked contrasts observed between mesostructured and planar Co-Pi/ $\alpha$ -Fe<sub>2</sub>O<sub>3</sub> photoanodes, the results here motivate a more comprehensive mechanistic investigation into the kinetic processes *specific* to mesostructured Co-Pi/ $\alpha$ -Fe<sub>2</sub>O<sub>3</sub> interfaces, and such experiments are currently underway in our laboratories.

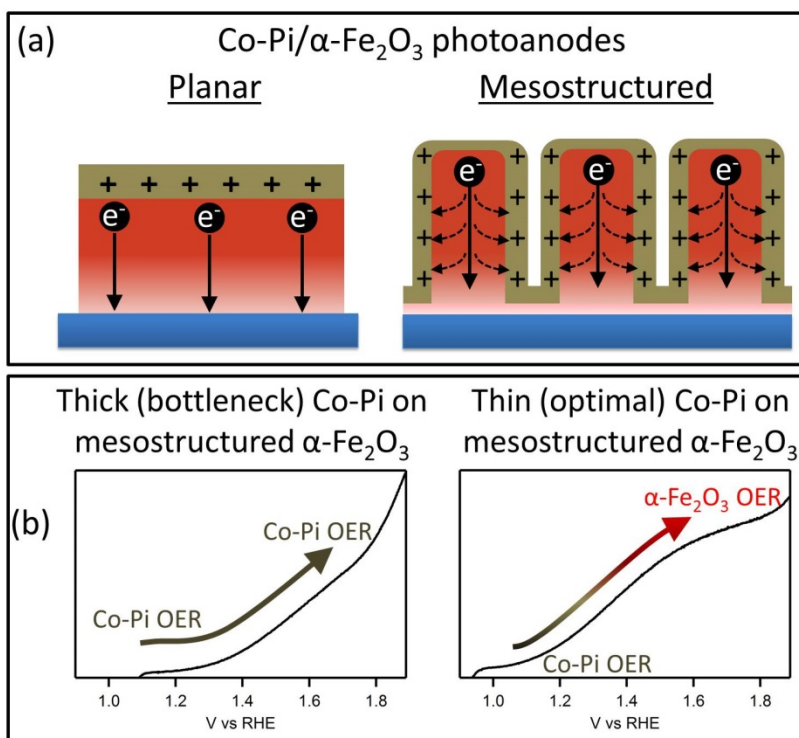


**Figure 6.** (a) Schematic comparison of contrasting surface electron-hole recombination processes during photoelectrochemical water oxidation by mesostructured and planar Co-Pi/ $\alpha$ -Fe<sub>2</sub>O<sub>3</sub> photoanodes. In planar photoanodes, electrons travel away from the SCLJ, and hence away from accumulated holes in the Co-Pi catalyst layer. This configuration minimizes surface electron-hole recombination. In mesostructured photoanodes, electrons spend more time traveling parallel to the SCLJ. When the Co-Pi catalyst layer is thick, it stores many oxidizing equivalents, and thicker Co-Pi deposition results in increased surface electron-hole recombination. (b) In PEC water oxidation by mesostructured Co-Pi/ $\alpha$ -Fe<sub>2</sub>O<sub>3</sub> photoanodes, the water-oxidation mechanism depends on the catalyst thickness and the applied potential. For thick Co-Pi catalyst layers, water oxidation is always performed by Co-Pi. For thin (optimized) Co-Pi layers, water oxidation at low potentials is performed by Co-Pi, whereas water oxidation at high potentials and high currents is performed directly by the  $\alpha$ -Fe<sub>2</sub>O<sub>3</sub> surface.

## Conclusion

Highly structured  $\alpha$ -Fe<sub>2</sub>O<sub>3</sub> photoanodes are susceptible to kinetic constraints when interfaced with thick Co-Pi catalyst layers. Optimization of the Co-Pi electrocatalyst thickness is necessary to achieve the maximum PEC efficiency at potentials  $<+1.6$  V vs RHE. Attenuation of photocurrent with increasing Co-Pi thickness arises due to interfacial recombination between photogenerated conduction-band electrons and accumulated Co-Pi holes ("kinetic bottleneck"). The importance of such recombination depends on the texture of the underlying photoanode. For mesostructured  $\alpha$ -Fe<sub>2</sub>O<sub>3</sub> photoanodes, the overall PEC efficiency is optimized with rather thin Co-Pi layers ( $\sim 2.5$  nm) because of this recombination. At these optimal Co-Pi thicknesses, PEC water oxidation can occur from both the Co-Pi electrocatalyst, which dominates at low applied bias, and directly from the  $\alpha$ -Fe<sub>2</sub>O<sub>3</sub> surface, which dominates at high applied bias. For planar  $\alpha$ -Fe<sub>2</sub>O<sub>3</sub> photoanodes, this recombination channel is no longer dominant, and very thick Co-Pi layers do not limit PEC performance.<sup>41</sup> These results clarify the mechanistic role that Co-Pi plays in improving the PEC performance of composite Co-Pi/ $\alpha$ -Fe<sub>2</sub>O<sub>3</sub> photoanodes,

and may have broad implications with respect to formation and optimization of related composite catalyst/photoelectrodes.

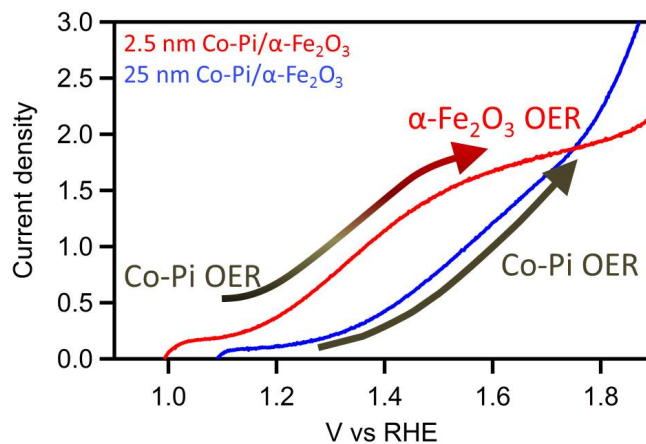
## Acknowledgments

This work was supported by the US National Science Foundation (CHE-1213283) and partially conducted at the UW Nanotechnology User Facility, a member of the NINN.

## References

1. A. Fujishima and K. Honda, *Nature*, 1972, **238**, 37-38.
2. N. S. Lewis and D. G. Nocera, *PNAS*, 2006, **103**, 15729-15735.
3. D. G. Nocera, *ChemSusChem*, 2009, **2**, 387-390.
4. A. J. Bard and M. A. Fox, *Acc. Chem. Res.*, 1995, **28**, 141-145.
5. W. Moomow, F. Yamba, M. Kamimoto, L. Maurice, J. Nyboer, K. Urama and T. Weir, in *IPCC Special Report on Renewable Energy Sources and Climate Change Mitigation*, eds. O. Edenhofer, R. Pichs-Madruga, Y. Sokona, K. Seyboth, P. Matschoss, S. Kadner, T. Zwickel, P. Eickemeier, G. Hansen, S. Schlömer and C. von Stechow, Cambridge University Press, United Kingdom and New York, NY, USA, 2011.
6. O. Khaselev and J. A. Turner, *Science*, 1998, **280**, 425-427.
7. M. Grätzel, *Nature*, 2001, **414**, 338-344.

8. D. K. Zhong, M. Cornuz, K. Sivula, M. Gratzel and D. R. Gamelin, *Energy Environ. Sci.*, 2011, **4**, 1759-1764.
9. A. Duret and M. Grätzel, *J. Phys. Chem. B*, 2005, **109**, 17184-17191.
10. F. E. Osterloh, *Chem. Mater.*, 2007, **20**, 35-54.
11. F. E. Osterloh, *Chem. Soc. Rev.*, 2013, **42**, 2294-2320.
12. R. F. G. Gardner, F. Sweett and D. W. Tanner, *J. Phys. Chem. Solids*, 1963, **24**, 1175-1181.
13. J. H. Kennedy and K. W. Frese, *J. Electrochem. Soc.*, 1978, **125**, 709-714.
14. M. P. Dare-Edwards, J. B. Goodenough, A. Hamnett and P. R. Trevellick, *J. Chem. Soc. Faraday Trans.*, 1983, **79**, 2027-2041.
15. F. Le Formal, K. Sivula and M. Grätzel, *J. Phys. Chem. C*, 2012, **116**, 26707-26720.
16. K. G. Upul Wijayantha, S. Saremi-Yarahmadi and L. M. Peter, *Phys. Chem. Chem. Phys.*, 2011, **13**, 5264-5270.
17. T. W. Hamann, *Dalton Trans.*, 2012, **41**, 7830-7834.
18. B. Klahr, S. Gimenez, F. Fabregat-Santiago, J. Bisquert and T. W. Hamann, *Energy Environ. Sci.*, 2012, **5**, 7626-7636.
19. B. M. Klahr and T. W. Hamann, *J. Phys. Chem. C*, 2011, **115**, 8393-8399.
20. M. Barroso, C. A. Mesa, S. R. Pendlebury, A. J. Cowan, T. Hisatomi, K. Sivula, M. Grätzel, D. R. Klug and J. R. Durrant, *PNAS*, 2012, **109**, 15640-15645.
21. M. Barroso, S. R. Pendlebury, A. J. Cowan and J. R. Durrant, *Chem. Sci.*, 2013, **4**, 2724-2734.
22. S. R. Pendlebury, A. J. Cowan, M. Barroso, K. Sivula, J. Ye, M. Gratzel, D. R. Klug, J. Tang and J. R. Durrant, *Energy Environ. Sci.*, 2012, **5**, 6304-6312.
23. W. D. Chemelewski, N. T. Hahn and C. B. Mullins, *J. Phys. Chem. C*, 2012, **116**, 5255-5261.
24. N. T. Hahn and C. B. Mullins, *Chem. Mater.*, 2010, **22**, 6474-6482.
25. H. Tang, M. A. Matin, H. Wang, T. Deutsch, M. Al-Jassim, J. Turner and Y. Yan, *J. Appl. Phys.*, 2011, **110**, 123511.
26. G. Wang, Y. Ling, D. A. Wheeler, K. E. N. George, K. Horsley, C. Heske, J. Z. Zhang and Y. Li, *Nano Lett.*, 2011, **11**, 3503-3509.
27. J. He and B. A. Parkinson, *ACS Comb. Sci.*, 2011, **13**, 399-404.
28. O. Zandi, B. M. Klahr and T. W. Hamann, *Energy Environ. Sci.*, 2013, **6**, 634-642.
29. K. Sivula, R. Zboril, F. Le Formal, R. Robert, A. Weidenkaff, J. Tucek, J. Frydrych and M. Grätzel, *J. Am. Chem. Soc.*, 2010, **132**, 7436-7444.
30. N. T. Hahn, H. Ye, D. W. Flaherty, A. J. Bard and C. B. Mullins, *ACS Nano*, 2010, **4**, 1977-1986.
31. R. H. Gonçalves, B. H. R. Lima and E. R. Leite, *J. Am. Chem. Soc.*, 2011, **133**, 6012-6019.
32. F. Le Formal, M. Grätzel and K. Sivula, *Adv. Funct. Mater.*, 2010, **20**, 1099-1107.
33. A. Kay, I. Cesar and M. Grätzel, *J. Am. Chem. Soc.*, 2006, **128**, 15714-15721.
34. D. K. Zhong, J. Sun, H. Inumaru and D. R. Gamelin, *J. Am. Chem. Soc.*, 2009, **131**, 6086-6087.
35. S. C. Riha, B. M. Klahr, E. C. Tyo, S. Seifert, S. Vajda, M. J. Pellin, T. W. Hamann and A. B. F. Martinson, *ACS Nano*, 2013, **7**, 2396-2405.
36. C. Du, X. Yang, M. T. Mayer, H. Hoyt, J. Xie, G. McMahon, G. Bischooping and D. Wang, *Angew. Chem. Int. Ed.*, 2013, **52**, 12692-12695.
37. M. W. Kanan and D. G. Nocera, *Science*, 2008, **321**, 1072-1075.
38. D. A. Lutterman, Y. Surendranath and D. G. Nocera, *J. Am. Chem. Soc.*, 2009, **131**, 3838-3839.
39. D. K. Zhong and D. R. Gamelin, *J. Am. Chem. Soc.*, 2010, **132**, 4202-4207.
40. M. Barroso, A. J. Cowan, S. R. Pendlebury, M. Grätzel, D. R. Klug and J. R. Durrant, *J. Am. Chem. Soc.*, 2011, **133**, 14868-14871.
41. B. Klahr, S. Giménez, F. Fabregat-Santiago, J. Bisquert and T. W. Hamann, *J. Am. Chem. Soc.*, 2012, **134**, 16693-16700.
42. F. Lin and S. W. Boettcher, *Nat. Mater.*, 2014, **13**, 81-86.
43. L. Trotochaud, T. J. Mills and S. W. Boettcher, *J. Phys. Chem. Lett.*, 2013, **4**, 931-935.
44. A. J. Cowan and J. R. Durrant, *Chem. Soc. Rev.*, 2013, **42**, 2281-2293.
45. T. W. Hamann, *Nat Mater*, 2014, **13**, 3-4.
46. J. G. McAlpin, Y. Surendranath, M. Dincă, T. A. Stich, S. A. Stoian, W. H. Casey, D. G. Nocera and R. D. Britt, *J. Am. Chem. Soc.*, 2010, **132**, 6882-6883.
47. D. R. Gamelin, *Nat. Chem.*, 2012, **4**, 965-967.



### TOC Graphic.

#### 20-word description:

Photoelectrochemical measurements on mesostructured Co-Pi/ $\alpha$ -Fe<sub>2</sub>O<sub>3</sub> composite photoanodes reveal evolving pathways of water oxidation with increasing Co-Pi thickness and applied bias.